Chemical Engineering Journal 482 (2024) 148959

Contents lists available at ScienceDirect

Chemical Engineering Journal

journal homepage: www.elsevier.com/locate/cej

Synergistic effect of Pd single atoms and nanoparticles deposited on carbon supports by ALD boosts alkaline hydrogen evolution reaction

Bilal Bawab [a], Sitaramanjaneya M. Thalluri [a,b], Eva Kolíbalová [a], Raul Zazpe [a,b], Ludek Jelinek [c], Jhonatan Rodriguez-Pereira [a,b], Jan M. Macak [a,b,*]

[a] Central European Institute of Technology, Brno University of Technology, Purkynova 123, 61200 Brno, Cech Republic
[b] Center of Materials and Nanotechnologies, Faculty of Chemical Technology, University of Pardubice, Nam. Cs. Legii 565, 53002 Pardubice, Czech Republic
[c] Department of Power Engineering, University of Chemistry and Technology, 166 28, Prague-6, Czech Republic

ARTICLE INFO

Keywords:
Atomic Layer Deposition
Pd single atom
Pd nanoparticles
Synergistic effect
Hydrogen evolution reaction

ABSTRACT

The synergistic effects between carbon supports and noble metal species of an electrocatalyst are known to effectively boost the alkaline hydrogen evolution reaction (HER). Herein, Atomic Layer Deposition (ALD) was employed to decorate carbon papers with Pd species comprising single atoms (SAs) and nanoparticles (NPs). Transmission electron microscopy analysis revealed the metallic nature and coexistence of Pd as SAs and NPs. The results of X-ray photoelectron spectroscopy supported the evidenced SA species, manifested as the Pd^{+2}. An increase in the electrochemical active surface area from 12.98 to 413.48 cm^{-2} was evidenced with increasing ALD cycles from 30 to 300c Pd and remained unchanged until 600c Pd. The exceptional overpotential for CP 600c Pd exhibits the lowest value of 4.55 mV, compared to previous reports for Pd electrocatalysts in a non-acidic environment, and confirms the synergistic effect of Pd SAs and NPs that plays a major role in enhancing alkaline HER.

1. Introduction

Hydrogen is a clean and renewable energy carrier that can be produced by electrochemical water splitting [1]. Among the catalysts studied for hydrogen evolution reaction (HER), platinum (Pt) has emerged as a standard due to its unique activity for HER [2,3], combined with low overpotentials [4–7] and very low Pt loading [8], in addition to other catalysts such as Ru [9–12], Ir [13], and Rh [14]. However, one of the problems that arise from the utilization of Pt as well as the other mentioned catalysts is their high cost and scarcity, which limit the large-scale application. In addition, the slower kinetics of Pt in alkaline electrolytes of approximately 3 times lower than that in acidic medium [4,15], triggered the search for substitution with similar or better performance for HER purposes. The focus on hydrogen production in an alkaline medium was more in demand because corrosion issues arise from the use of an acidic environment during the long term HER process [16]. Therefore, the development of alternative catalyst is needed that can perform excellent in alkaline media.

To address these challenges, palladium (Pd) emerges as a promising alternative to Pt showing good catalytic activity and long-term chemical stability during HER [17,18], especially in alkaline media [19]. One strategy to achieve this is to combine Pd single atoms (SAs) and nanoparticles (NPs) on suitable supports, which can create synergistic effects between the two types of Pd species and enhance the catalytic performance of Pd. A study [20] demonstrates the synergistic activity by anchoring the Pd species on carbon self-doped graphitic carbon nitride (CCN_x). The mechanism reveals that the synergy of the Pd species as electron trapping sites significantly lowers the energy barrier of H* activation. On the other hand, Pd can form alloys and hydrides with other metals to enhance its activity and stability for HER [21,22]. Previous studies [23] demonstrate a significant low overpotential for Pd NPs of approximately 80 mV at a current density of 100 mA cm^{-2} related to the porous Pd nanoparticle assemblies. In some other cases such as Pd-Cu-H [24] that show high catalytic performance and attributes this to the better H* adsorption and activation on the Pd surface. Moreover, Zheng et al. [25] reported that with increasing the size of Pd nanoparticles from 3 to 19 nm, higher HER exchange currents were obtained in both acidic and alkaline medium due to the decreasing trend of surface defects with increase in NPs size.. Furthermore, the proximity of active species on a support introduces the intriguing concept of the

* Corresponding author.
E-mail address: jan.macak@upce.cz (J.M. Macak).

https://doi.org/10.1016/j.cej.2024.148959
Received 4 August 2023; Received in revised form 11 January 2024; Accepted 19 January 2024
Available online 21 January 2024

hydrogen spillover effect [26,27], wherein H* species can diffuse from donor to acceptor sites, potentially enhancing the catalytic activity. This phenomenon becomes pivotal when considering the cooperative synergy between single atoms (SAs) and nanoparticles (NPs) in catalysis. Recent research [28–30] has illuminated the possibility of integrating SAs and NPs on the same support, creating a platform for novel catalytic interactions. This synergy holds the potential to catalyze reactions that may be challenging for either SAs or NPs alone.

Carbon-based materials [31,32] are widely used as supports for electrocatalysts, as they are low cost, have high stability and good electrical conductivity. Among them, carbon papers (CPs) have a high porosity and surface area [33], which can facilitate catalyst distribution, the mass transport of reactants and products during HER, good electrical conductivity known to enhance the charge transfer, and mechanical stability to support durability of catalysts for practical long term HER applications. Therefore, CPs are a promising substrate for electrocatalysis. In addition, CP can be easily treated with an acidic solution to introduce functional groups such as carboxylic acid, hydroxyl, and carbonyl on the surface of carbon substrates [34,35], which can increase their wettability and improved affinity with metal precursors during deposition process. The degree of acid treatment can affect the hydrophilicity of carbon substrates, as well as their mechanical, thermal, and electrochemical properties.

Our study aims to explore the synergistic interplay between Pd single atoms and nanoparticles on a suitable support for enhanced HER performance. We employed acid-treated CPs as substrates for the deposition of Pd species using Atomic Layer Deposition (ALD) [36], resulting in the simultaneous presence of Pd species as both single atoms (SAs) and nanoparticles (NPs). Furthermore, along the manuscript, Pd SAs and NPs are collectively referred to Pd species. Different number of ALD cycles (N_{ALD}) comprising of 30, 45, 60, 75, 150, 300, 450 and 600 were applied to exploit the presence of Pd species and related activity for alkaline HER. High-angle annular dark field scanning transmission electron microscopy (HAADF-STEM) images evaluation confirmed the coexistence of Pd species as SAs and NPs on CPs starting from N_{ALD} = 75c Pd. The electrochemical measurements showed low overpotential values of 4.55 mV vs reversible hydrogen electrode (RHE) along with low charge transfer resistance (R_{ct}) of 0.65 Ω at 20 mV of applied potential for the CP 600c Pd sample. To evaluate the HER activity of the catalysts, the electrochemical surface area (ECSA) and the number of available active sites were assessed. Long-term stability tests employing a staircase chronopotentiometry at different current densities show excellent stability of CPs decorated with Pd nanoparticles for duration of 15 h in comparison to Pt developed by similar ALD route [12]. Accelerated degradations tests at high scan rate in a limited potential window further confirmed the excellent durability of the developed CP-600c Pd sample.

2. Experimental

2.1. Electrode preparation/treatment

Commercial carbon papers (CP) were treated with a 1:3 mixture of HNO_3 and H_2SO_4 for 15 min under sonication at 60 °C. The acid treatment is known to enhance the hydrophilic nature of the carbon substrates [12,37]. Subsequently, the CPs were thoroughly rinsed with distilled H_2O several times. The resulting CPs were employed in ALD for Pd deposition.

2.2. Atomic Layer deposition of Pd

Pd species were deposited onto treated CPs using a TFS 200 ALD reactor. Palladium(II)hexafluoroacetylacetonate $Pd(C_5HF_6O_2)_2$ and formalin were used as the precursor and co-reactant. The Pd precursor was heated to 65 °C and the deposition process temperature was 200 °C. The ALD cycle was defined by a sequence of Pd pulse (2 s), N_2 purge (30 s), formalin pulse (1 s), and N_2 purge (30 s). A preliminary step of 250 ms of Pd precursor with a 30 s N_2 purge and 1 s formalin with a 30 s purge for 20 cycles was applied to lower the Pd precursor consumption. This is because in early stages of the ALD process, the volatility of the Pd precursor is significantly higher, which can lead to issues related to excess Pd precursor wastage and control. By distributing the initial pulses in this manner, we achieve better control over precursor consumption, ensuring that the reactor is always with saturated with provided pulse duration. Thus, the total number of ALD cycles were calculated taking into consideration of initial 20 cycles (20 + x cycles = Total number of cycles). Different "number of Pd ALD cycles (N_{ALD})" were performed on CPs with: N_{ALD} = 30, 45, 60, 75, 150, 300, 450, and 600 cycles.

2.3. Characterization methods

Pd deposited CPs were characterized using Scanning Electron Microscopy (SEM, FEI Verios 460L) and compared to the Blank CP. High-resolution Transmission Electron Microscope (HRTEM, Titan Themis 60–300, Thermo Fisher Scientific,) operated at 300 kV was also employed. HRTEM is equipped with a Cs image aberration corrector, high-angle annular dark field scanning transmission detector (HAADF-STEM), and Super-X energy dispersive X-ray (EDX) spectrometer with four 30 mm^2 windowless detectors for STEM-EDX analysis to evaluate the elemental composition and the morphology of the deposited Pd. The crystallinity was assessed using X-ray diffraction XRD Rigaku Smartlab 3 kW diffractometer equipped with Cu-Kα1 radiation source (λ = 1.54060 Å), using 40 kV and 30 mA as beam energy source. The patterns were collected in the 2θ range (10 − 90°) and at a scanning rate of 0.01 °/step with a speed of 4 °/min. To verify the surface chemical composition before and after electrochemical measurements, X-ray photoelectron spectroscopy (XPS) analysis was performed using Kratos Analytical Axis Supra instrument, with Al-Kα monochromatic X-ray source (hν = 1486.69 eV). The acquired spectra were further fitted using CasaXPS software and referenced to the sp^2 species in C 1 s signal at 284.0 eV, in order to perform the binding energy scale correction. Pd 3d spectra were fitted with asymmetric Lorentzian function LA (0.95, 2, 150) for metallic state (Pd^0) and mixed Gaussian-Lorentzian functions GL (30) for Pd oxides and Pd plasmon loss. Inductively coupled plasma - optical emission spectroscopy (ICP-OES) analyses were performed using (Thermo-Fischer iCAP 7400) axial mode, RF power 1150 W, 340.458, 324.270, and 363.470 nm after dissolving the CP@Pd in a solution of 1:3 mixture of HCl and HNO_3 in a microwave reactor (Multiwave 5000 – Anton-Parr).

2.4. Electrochemical analysis

Electrochemical measurements were performed using the Autolab VIONIC potentiostat supported by INTELLO software, where 1 M KOH was used as the electrolyte. A calibrated Ag/AgCl (3 M KCl = 0.210 V versus RHE) used as a reference electrode, graphite rod was used as a counter electrode and CPs with and without Pd were used as a working electrode. Linear sweep voltammetry (LSV) was performed at a scan rate of 2 mV s^{-1}, where the Tafel slopes are plotted after 100 % iR correction. Electrochemical Impedance Spectroscopy (EIS) measurements were evaluated at 20 mV overpotential using 10 mV as an AC perturbation potential, within a frequency range of 10^{-2} to 10^5 Hz. Copper underpotential deposition method was used to estimate the electrochemical surface area (ECSA) at a scanning rate of 10 mV s^{-1} and compared for all samples. Stability measurements were performed by 15 h long chronopotentiometry. Stability measurements were also performed by accelerated degradation test by subjecting the catalyst to 2500 repetitions of cyclic potential sweeps in the potential range of ± 50 mV at a higher scanning rate of 50 mV s^{-1}, in comparison to activity measurements of 2 mV s^{-1}. All the potentials presented are given versus RHE unless otherwise stated.

3. Results and discussion

3.1. Morphological and chemical characterization

Figure S1 shows SEM images of CP blank and ALD decorated CPs with Pd species. For reference, images of CP decorated with Pt nanoparticles are shown as well. The CPs decorated with Pd species by different N_{ALD} from 0 to 600c Pd are presented. Samples with $N_{ALD} = 75$, 150, and 300 (Fig. S1 b-d) exhibit sparse and scattered Pd NPs on the surface of CPs. However, for $N_{ALD} \geq 450$ and 600 (Fig. S1e,f), the coverage of Pd NPs becomes more evident, in terms of size and distribution. During the ALD process for noble metals, the initial nucleation stage is followed by atom aggregation, leading to the formation of atomic clusters, which subsequently develop into nanoparticles [12,38,39]. However, the utilization of acid-treated carbon substrates offers several advantages, including the provision of additional active sites for Pd precursor adsorption and facilitating enhanced Pd nucleation and growth [40]. A nucleation delay can be noted during the ALD process with the Pd precursor employed, which is in line with reported observations due to difficulty in removal of re-adsorbed Pd precursor ligands (hexafluoroacetylacetonate) on the support [41]. **Fig. S1 g,h** provides morphological overview of ALD decorated CP 50c Pt. N_{ALD} of 50c was chosen for Pt, taking into consideration of previous reports [12,42]. The ALD of Pt on CPs shows an excellent coverage.

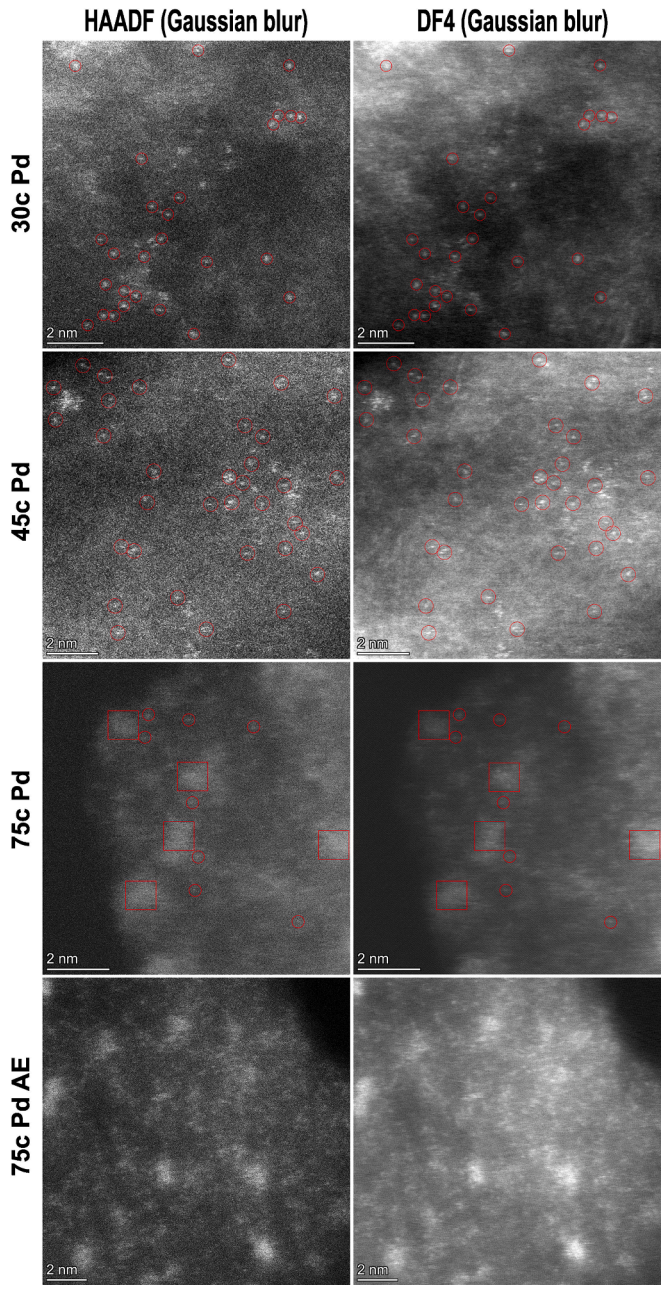

Fig. 1. HAADF-STEM images (left column) and Dark field (DF4) (right column) images for 30, 45, and 75c Pd (before and after electrochemical measurements (AE)).

More in-depth information about the Pd species on CPs was obtained by HRTEM studies, where the elemental composition and indexing of crystalline lattice of Pd NPs were collected. Fig. 1 shows the high-angle annular dark-field imaging (HAADF) and dark field (DF4) images, providing further information about the presence of Pd species. The CP 30c Pd sample showed no traces of nanoparticles, but only single atoms (SAs) that were marked by red circles in the relevant images. Increasing the N_{ALD} to 45c cycles showed a mixture of SAs and SA clusters (marked by a red square, while no nanoparticles (NPs) were observed. When the N_{ALD} increased to 75 cycles, the presence of NPs was observed in addition to SAs and SA clusters. The presence of SAs in addition to NPs on CP 150, 300, and 600c Pd was also approved by TEM in Fig. S2a-c with further XPS analysis provided later.

Fig. S3a-i shows the elemental distribution by combining HAADF-STEM imaging and STEM-EDX for the CP 600c Pd sample, providing elemental mapping for C-K, O-K, Pd-L, and ovelapped C + O + Pd maps, respectively. From the mapping, a significant reduction in oxygen distribution at Pd NPs location suggesting dominance of metallic nature from ALD depositied Pd. This was further confirmed by the STEM-EDX line scan that was conducted to take advantage of isolated Pd NP on CP as shown in Fig. S3e. Fig. S3f provides details of the graphical weight percentages along the analysed line scan (Fig. S3e) for C, O and Pd. The trend of O line when compared with Pd line were inversly related providing a cross confirmation of metallic nature of the ALD deposited Pd. HAADF-STEM imaging from Fig. 1 revealed the presence of SA for lower NALD sample (CP 30c Pd), clusters (CP 45c Pd) and NPs staring from 75c Pd, which is in accordance to the ALD noble metal deposition profile, as suggested before. The distribution density of individual species of Pd increases with increase in NALD. As shown in Fig. S4, the NPs sizes exhibit a gradual growth with increasing the ALD cycles, showing average sizes of 0.7, 1.3, 7.1, 8.1 nm size for 75c, 150c, 300c, and 600c Pd, respectively. The Fast Fourier Transformation (FFT) pattern obtained from a single Pd NP (Fig. 3g-i) reveals distinct diffractions represented by marked spots. These diffractions correspond to cubic structure and to (3 1 1), (0 0 2) and (1 1 1) planes with d-spacings of 0.12, 0.19, and 0.23 nm, respectively, which is inline with XRD analysis.

The crystal structure and phase composition of the CPs modified with Pd species were investigated by X-ray diffraction (XRD). **Fig. S5** shows the XRD patterns of the CPs decorated with Pd using different N_{ALD}. The Pd peaks are barely visible for $N_{ALD} = 75$ (indicating a low Pd loading on the surface) and become more evident from $N_{ALD} \geq 150$, suggesting crystalline nature and a higher Pd loading with increased N_{ALD}. However, some of the Pd peaks are partially overlapped by the CP substrate peaks evidenced at higher N_{ALD} (300 to 600 cycles), especially around 44.59°. The ALD Pd has a cubic crystal structure with diffraction peaks matching well with the standard reference pattern (PDF 01–087-0641). The characteristic Pd peaks at $2\theta = 39.39$, 45.8, 66.7, and 80.4° correspond to the (1 1 1), (2 0 0), (2 2 0), and (3 1 1) lattice planes, respectively. The diffraction peaks intensity for Pd increases with increasing the ALD cycles with lower half width of full maxima indicating a gradual increase in the crystallite size from 5.03 to 5.61 nm for CP 300c Pd to CP 600c Pd respectively (**Equation (S1)**, **Table (S1)** in supplementary information).

XPS analysis for CP 600c Pd was carried out to gain more insight about the surface chemical composition. Fig. 2a shows the wide-scan XPS survey spectrum revealing the presence of C, O, and Pd elements, where the C peak was used to correct the binding energy scale of the

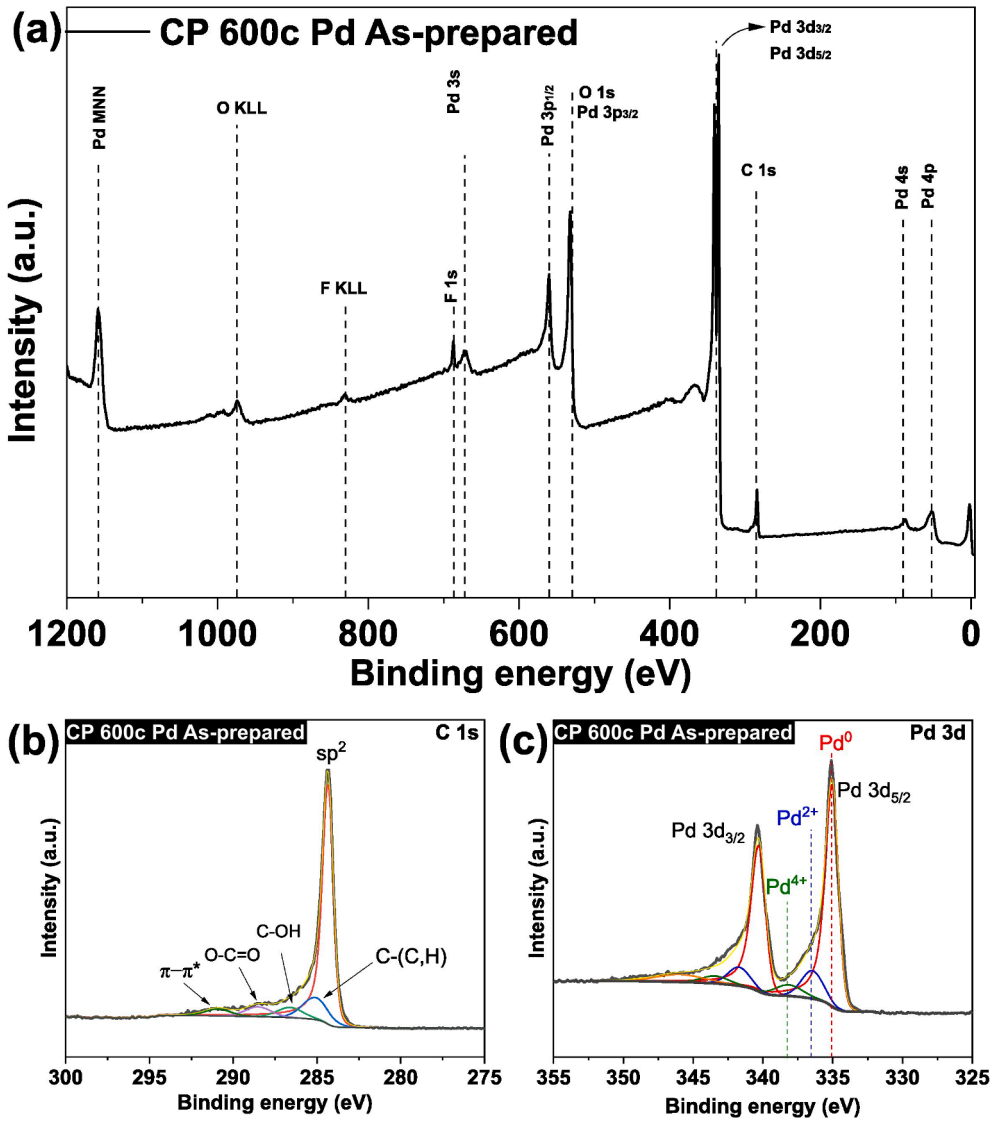

Fig. 2. XPS spectra of CP 600c Pd sample: a) wide survey spectra; b) and c) high-resolution spectra for C 1 s and Pd 3d, respectively.

spectra. The minor peak observed for F arise from the fact of the re-adsorbed Pd precursor fragments (containing F species) on the substrate as explained before. On the other hand, Pd 3d two sublevels shown in Fig. 2c exhibits a significant amount of Pd in metallic form, as shown in the red fitted curves at 335 and 340.3 eV. Here, the peak energy splitting for Pd 3d spin–orbit doublets appears to be around 5.26 eV, similar values to those reported in the literature [43,44]. The shoulder peaks fitted in blue curves and located around 336.4 and 341.6 eV were denoted as Pd^{2+} and they correspond to the bonding with surface active O linked species, such as (C-OH and O-C = O) in the 286–289 eV range originated as a result of CP pretreatments resulting in SAs [45,46] and also a minor amount from O that forms PdO as a result of sample exposure to air, in-line with previous reports [44]. The olive peaks correspond to Pd^{4+} species centered at 338.2 and 343.4 eV. The reported PdO binding energy for CP 600c Pd was around 336.4 eV, close to the values reported for the surface oxides in the literature [47–50]. It is important to note that the bulk oxides typically exhibit lower binding energies. This is supported by the presence of Pd single atoms detected by TEM, which contributes to the presence of shoulder Pd peak [45,51,52] (represented as Pd^{2+}). **Table S2** provides a quantitative assessment for the deconvoluted high resolution spectra of Pd peak, confirming atomic percentages of 79.8 and 13.5 for Pd^{0} and Pd^{+2} components, respectively.

3.2. HER activity of CP@Pd

During the H_2O dissociation on the surface of Pd, OH^- and H* are formed as intermediates, where the H* will participate in the production of H_2. Polarization experiments were conducted to investigate the performance of CPs decorated with Pd species for HER activity. The LSV analysis was performed in 1 M KOH solution with additional iR correction as shown in Fig. 3a. The LSV curves show excellent HER activity, with a blank CP sample shown as a reference. It is important to assess the overpotential for each electrode required to reach a cathodic current density of 10 mA cm^{-2}. The data in Fig. 3a shows that the presence of only SAs as a catalyst on the lowest N_{ALD} (30c Pd) results in much higher overpotential of 313.6 mV. As the SA density increases, SA clusters start to form, as shown in Fig. 1 for 45c Pd, leading to lower overpotentials. A substantial decrease in overpotential values was obtained for 75c Pd ALD, leading to as low overpotential as 28.8 mV, a much lower value than the commercial Pd/C and Pt/C reported with a value of 175 and 72 mV [53]. Increasing the Pd loading quantity to 450 and 600c ALD shows a gain in overpotentials recording 5 and 4.55 mV, respectively. The observed overpotentials are much lower than the values reported in the literature [23,24]. This indicates that the treated CPs with ALD decorated Pd species have supported to facilitate faster electron transfer and H_2O reduction.

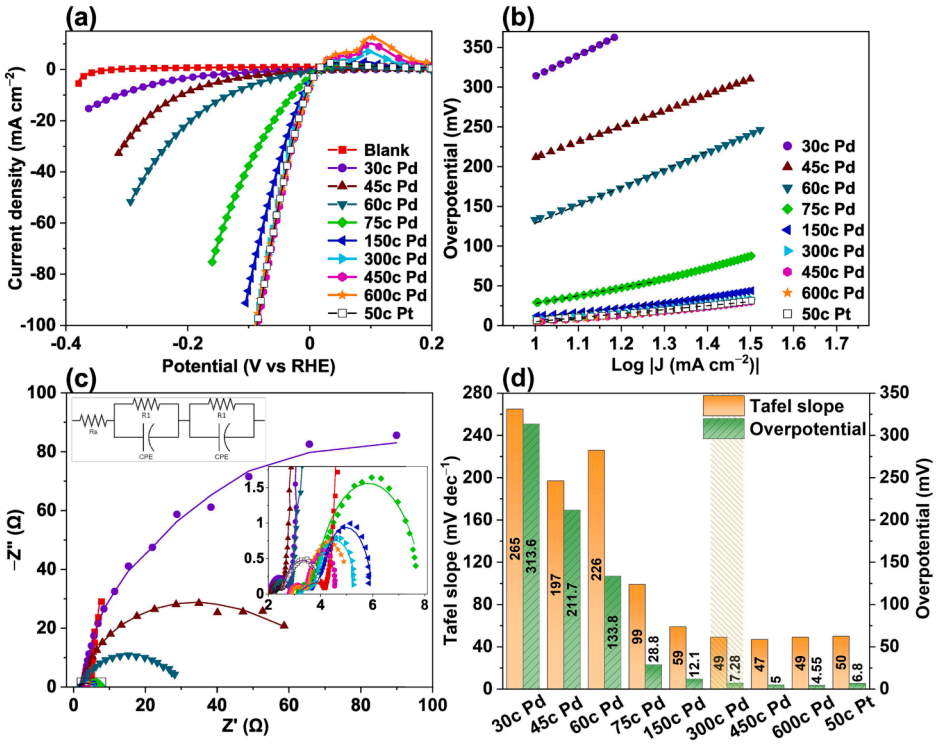

Fig. 3. Electrochemical HER analysis: a) iR corrected LSV; b) Tafel slope analysis in the current density range of (10 – ~30 mA cm^{-2}); (c) EIS experimental and fitting curves data; d) comparitive bar plot for Tafel slopes and overpotential values for CP Pd and CP 50c Pt samples.

Tafel analysis was used as a parameter to elucidate the reaction mechanism and kinetics of the HER taking place at Pd species surface. This can provide a clear understanding of the Pd species behavior, and the mechanism involved within the HER. According to previous findings [54–56], Tafel slope for Pd NPs can range from 40 to 130 mV dec^{-1}. In the present case, the CP@Pd species including NPs, such as N_{ALD} 75c, 150c, 300c, 450c, and 600c, have Tafel slopes of 99, 59, 49, 47, and 49 mV dec^{-1} respectively, as shown in Fig. 3b indicating that the reaction kinetics follow Volmer-Heyrovsky mechanism. However, the lower Pd loaded CPs with SAs showed substantial increase in Tafel slope value recording 265, 197, and 226 mV dec^{-1} for 30, 45, and 60c Pd, respectively. The improved kinetics of Pd species on CP increased with increasing N_{ALD} up to 300c Pd, while higher N_{ALD} (300, 450, and 600) showed very similar Tafel slopes. The N_{ALD} of Pd deposition influenced the Pd species density, which played a critical role for alkaline HER performance. According to our understanding, the optimal density of Pd species for HER performance was observed with N_{ALD} 300c and stabilizes with further increase until 600c Pd. However, the Tafel slope obtained from N_{ALD} 300 to 600c Pd, is comparable to some of the best reported values for Pd-based electrocatalysts [53]. For a comparative purpose, Tafel slope values for CP 50c Pt overlayed in Fig. 3b showing a value of 50.14 mV dec^{-1}, which is close to those recorded for the higher palladium loading of 450 and 600c Pd.

The initial H_2O dissociation has been widely considered as bottle neck problem for alkaline HER. A previous study [57] provides valuable insights into this process through comprehensive investigations, utilizing both Density Functional Theory (DFT) calculations and Extended X-ray Absorption Fine Structure (EXAFS) measurements. These analyses elucidate the role of Pd nanoparticles (NPs) as active centers in facilitating H_2O dissociation, leading to the generation of key reactive species, active Hydrogen atoms (H*) and hydroxyl groups (OH^-). Our study builds upon these findings by investigating the impact of NPs in the context of our experimental framework. We observed a pronounced correlation between the presence and concentration of NPs and the enhancement of H_2O dissociation. The increased footprint of NPs in the samples of CP@Pd with the rise in N_{ALD} concentration suggests a relation with improved H_2O dissociation, resulting in the enhanced generation of reactive H* species. Our findings support and further demonstrate the significance of NPs in the H_2O dissociation process during the alkaline HER. By integrating the results from reference [56] with our own experimental observations, we aim to provide a more complete understanding of this critical reaction mechanism.

The generated H* on the Pd NPs surface are expected to spillover onto the available SAs of Pd, where the Volmer-Heyrovsky mechanism (explained in the Supplementary Information) occurs. Recently, the unprecedented activity for HER was demonstrated by SA of Pd [46] in comparison to SA of Pt and Au, when employed as cocatalysts on TiO_2 photocatalyst. This enhanced activity of Pd SA was mainly due to more prominent charge localization according to DFT analysis [46]. Similarly, in the current context, the adsorbed H* on Pd SAs active sites reacts with the neighboring H_2O molecule, such that the proton from the H_2O molecule combines with the adsorbed H* to form Hydrogen molecule (H_2). This overall synergistic effect between the Pd NPs and SAs represent the enhanced HER performance of the CP@Pd, the main highlight of this work.

Charge transfer analysis was carried out by employing EIS and is presented in Fig. 3c. Fitting the experimental EIS data was performed using a simple equivalent circuit model, consisting of only five elements. The circuit fits the experimental data well, as evidenced by the excellent agreement between the experimental data and the fitted data for all CPs decorated with Pd species. The fitting results illustrate the values of R_1, R_2/Q_1, and R_3/Q_2 indicating that the electrical properties of the CP substrate and the Pd species on CP in relation to the N_{ALD}. The values obtained from the fitting (**Table S3**) showed that the resistance (R_s) of the samples ranged from 2 to 3.19 Ω used for iR correction. The first parallel component (R_2/Q_1) illustrates the charge transfer kinetics of the carbon substrate, with resistance values varies from 0.57 to 1.69 Ω. While the second component (R_3/Q_2) illustrates the charge transfer resistance at the interface of catalytically active Pd species. The R_{ct} decreased significantly from 178.28 to 0.65 Ω with increasing N_{ALD} from

30 to 600c Pd. The decrease in R_{ct} with increase in N_{ALD}, confirms improvement on the electrical properties and thus the HER activity of CP@Pd. The observed increase in capacitance can be related to increase in the amount of adsorbed H* on the Pd surface [58]. The CP 50c Pt sample was used to perform a comparative assessment of HER under the same conditions. Fig. 3d provides a comprehensive view of the activity profiles of the respective electrodes, as depicted by the comparative bar plot of overpotentials and Tafel slopes. Pt displays an overpotential of 6.8 mV, which falls within the range of overpotential values observed for CP 300c and CP 450c Pd.

3.3. Number of active sites and their role in performance enhancement

For supported catalysts such as SA, NPs or thin films on flat or high surface area supports, the calculated electrochemical surface area (ECSA) used to determine the active catalyst surface area. One of the common methods to evaluate the ECSA of Pd noble metal electrocatalysts is to use the reduction peak of the oxide layer formed on the metal surface [59]. However, this method need to be carefully considered basing on the available Pd facets and potential range chosen in the CV scan to oxidize and reduce the Pd species available on the surface [60].

An alternative method that can overcome these drawbacks is to use under potential electrodeposition of Cu with a further stripping of deposited monolayer of Cu. Therefore, the ECSA for CP Pd electrodes was determined by integrating the Cu stripping peak, as shown in **Fig. S6(a-f)**. The initial choice of the applied potential was evaluated by performing a series of LSV initiating from different potentials as shown in **Fig. S6a**, where 0.31 V was used for Cu monolayer deposition. There is a large distinction of bulk Cu deposition and monolayer Cu deposition with applied initial potential for LSV. This potential for monolayer deposition was adopted for the rest of the CP samples decorated with Pd. As shown in Fig. 4a, ECSA increased gradually from 12.98 to 413.48 cm^2 as the N_{ALD} increased from 30c to 300c. Further increase in the N_{ALD} from 300 to 600c shows approximately close ECSA values of 413.48, 395.63, and 411.98 cm^2 respectively, which agrees with the overpotentials recorded from LSVs. The increase of ECSA values with increasing N_{ALD} can be attributed to the higher active surface area of Pd species exposed to the electrolyte [61–63]. Furthermore, the number of active sites (N) shown in Fig. 4b increases from 1.72×10^{16} to 5.47×10^{17} by increasing the N_{ALD} from 30 to 300c Pd, and with further increase in N_{ALD}, the number of active sites remains relatively stable with values of 5.47×10^{17}, 5.23×10^{17}, and 5.45×10^{17} for 300, 450, and 600c Pd respectively, which is proportional with ECSA obtained values. Therefore, the saturation of the available active sites starts to occur at $N_{ALD} = 300c$.

To gain deeper insight about the intrinsic activity of Pd species, the turnover frequency (TOF) was quantified as a pivotal marker of intrinsic catalytic performance [64]. TOF measures the efficiency of a catalyst active site for a specific reaction [65]. While our study has emphasized the ECSA values and the quantification of active sites within the Pd species, it is crucial to examine the TOF values, as depicted in Fig. 4c. Our analysis reveals that the TOF values for Pd species fall within the range of 0.15 to 0.22 $H_2\ s^{-1}$ at 30 mV, however, by applying $N_{ALD} \leq 45c$ Pd, TOF value start to decline. This suggest that apart from having only SAs as a catalyst, as observed in 30 and 45c Pd, all the samples share similar HER reaction strategy and only the increase in the number of active sites directly influences the low overpotentials observed with LSV measurements. It is worth noting that our determination of ECSA through copper monolayer deposition involve both single atoms (SAs) and nanoparticles (NPs) present as a catalyst. This is a critical point of consideration in our TOF calculations. ICP-OES analysis was carried out for all samples that include NPs to determine the Pd metal loadings. The estimated weight percent (wt. %) of Pd as shown **Fig. S7** follow a linear increase of 1.61, 4.4, 9.87, 12.82, and 15.88 for CP 75, 150, 300, 450 and 600c Pd, respectively. However, the activities found for the CP@Pd samples are mostly correlated with the number of active sites, rather than the loading mass, due to the fact that all the loading mass will not

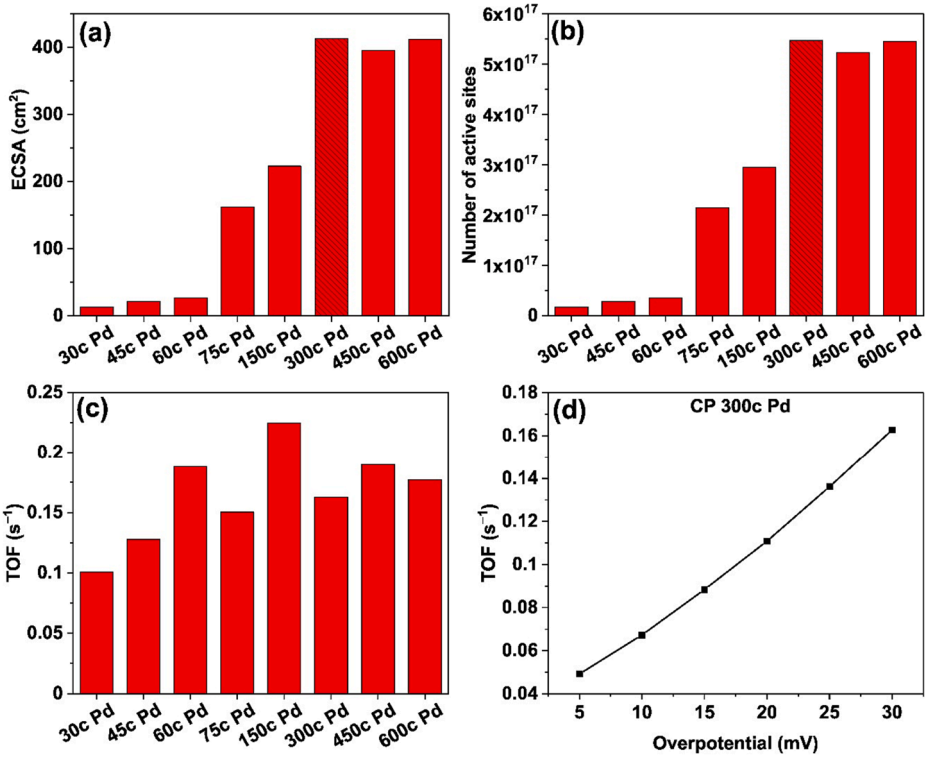

Fig. 4. a) Electrochemical surface area (ECSA); b) number of active sites; c) turnover frequency (TOF) for 75, 150,300, 450, and 600c Pd at 30 mV overpotential; d) TOF for CP 300c Pd at different overpotentials, where the connecting line used for eye guidance. The pattern highlighted columns in (a) and (b) referred to CP 300c Pd indicate the threshold at which the HER performance gets saturated.

participate in the HER catalytic activity. It is possible to have confusion when relating the improved overpotentials with the decrease in SAs as N_{ALD} increases. Due to agglomeration, the increase in NPs size as depicted in **Fig. S4** lowers the probability of SAs presence as the NPs are consuming larger area of the CP surface. However, NPs exhibit a stronger interaction with water molecules than SAs as described [57]. Thus, the increase in the NPs quantity in the higher Pd-loaded CPs resulting in producing more hydrogen atoms, compensating for the drop in Pd single atoms.

3.4. Stability evaluation by staircase chronopotentiometric and accelerated degradation tests

How well an electrocatalyst works in practice depends largely on how long it can maintain stable activity over the time. To further investigate the stability of CP 600c Pd, chronopotentiometric measurements for CP 600c Pd were assessed for 15 h with steps of different current densities, as shown in Fig. 5a. The overpotentials remained stable during the initial 12 h at an applied current density of 10 mA cm^{-2}. Stepping the current density to 20, 50, and 10 mA cm^{-2} and maintained for 1 h did not hamper the overpotential with change in current densities. In fact, a slight gain of 3 mV was observed during the final 1 h stability measurement employing 10 mA cm^{-2}. For comparison, 50c Pt ALD coated CP stability measurement was carried out under the same conditions. A 10 mV rise in overpotentials were observed during the initial 12 h measurement at 10 mA cm^{-2}. Further changing the current densities to 20, 50, and 10 mA cm^{-2} displayed an average of 5, 2, and 6 mV higher overpotential respectively, when compared with Pd.

LSV was performed for CP 600c Pd before and after the long-term stability test, as shown in Fig. 5b. The overpotential increased from 8.27 mV to 15.2 mV after the stability test, while the overpotential of CP 50c Pt increased from 6.8 mV to 17.6 mV, as shown in Fig. 5c. This is around 6.9 mV change for CP 600c Pd, compared to 10.8 mV for CP 50c Pt overpotential change, suggesting that CP@Pd retain more activity after the stability test. Part of the recorded change could be correlated to the loss of some fragments of the electrode due to H_2 bubbles generated on the surface. TEM (**Fig. S8**) and XPS (**Fig. S9 and Table S2**) analyses, carried out after the stability measurement, did not show any significant change in the morphology and oxidation state of the samples. This is a promising result, as it suggests that the Pd species are stable and resistant to degradation under the test conditions. HR-TEM imaging and FFT pattern analysis in **Fig. S10a,b** showed that the Pd nanoparticles had a matching cubic crystalline structure with the (311), (002) and (111) planes with d-spacings of 0.12, 0.19, and 0.23 nm respectively, after stability measurements.

Additionally, the stability of the electrodes was evaluated in dynamic conditions, where electrode was subjected to repeated CV at higher scan rate [66]. An accelerated degradation test was performed for the CP 600c Pd sample for 2500 cycles in a potential range of ± 50 mV and a scanning rate of 50 mV s^{-1}. The electrode displayed excellent stability, with 1 mV gain in the overpotential between the polarization curves collected before and after test, as observed in Fig. 5d. A comparative summary of the relative overpotentials and Tafel slopes achieved in this work are listed in **Table S4**, along with results from other studies. The low values recorded for CP 450 and 600c Pd suggest excellent HER performance by highlighting the importance of using treated CPs and

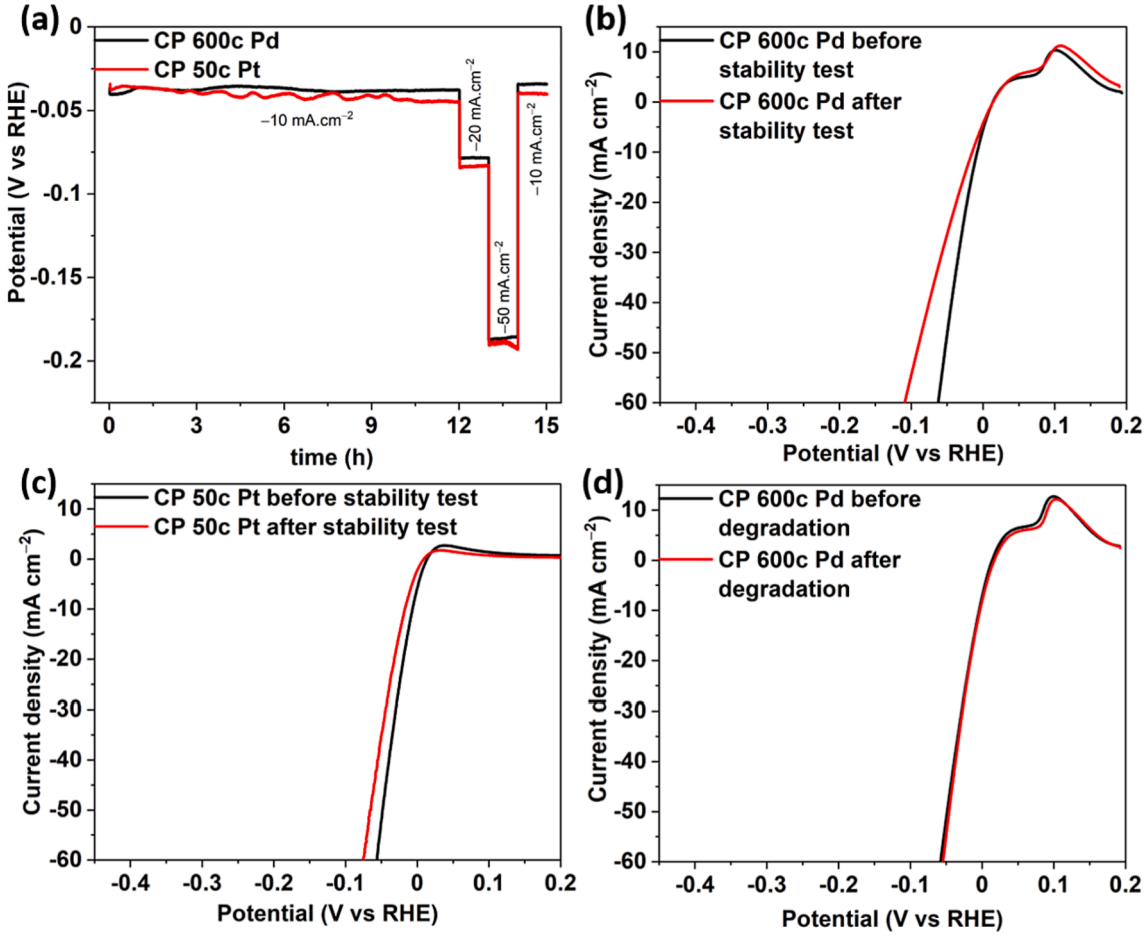

Fig. 5. Stability measurement: a) straicase chronopotentiometry; b) LSV before and after stability test for CP 600c Pd; c) LSV before and after stability test for CP 50c Pt; d) LSV before and after degradation test for CP 600c Pd.

ALD technique to obtain Pd species comprising of SA and NPs having unique synergistic activity and excellent stability for the alkaline HER.

4. Conclusion

ALD was employed to decorate Pd species on activated CPs. The coexistence of both SAs and NPs plays the major role in improving the HER activity in the alkaline medium. The NPs play a crucial role in H_2O dissociation and the HER process proceeds in the presence of SAs. The combination of these parameters with an increased number of active sites by increasing N_{ALD}, ushered to an efficient and highly active catalyst with overpotentials of 4.55 mV. The overpotentials were comparable to CP@Pt catalyst prepared in similar fashion. However, the presence of only SAs on the lower Pd loaded CPs show poor HER activity. Moreover, the developed CP@Pd catalyst showed excellent stability for prolonged duration with no significant loss in activity, as confirmed by various characterization techniques (XRD, XPS, HRTEM). Overall, this work highlights the synergistic effect of SAs and NPs of Pd on a conducting support as highly efficient and stable electrocatalysts for alkaline HER.

CRediT authorship contribution statement

B.B., and S.M.T. contributed equally to the paper. B.B., S.M.T. and J.M.M. conceived this study. S.M.T. and R.Z., tuned carbon paper pretreatments and ALD process parameters. B.B. carried out XPS, XRD and electrochemical measurements and analysis. E.K. conducted HRTEM measurements accompanied with EDX elemental mapping. J.L. conducted ICP-OES measurements. J.R.P. conducted additional ALD processes and carried out new XPS measurements and fittings. J.M.M. Resources, Project administration, Funding acquisition. All authors discussed the manuscript and the results. The manuscript was written by B. B., S.M.T. and J.M.M. All authors have given approval to the final version of the manuscript.

Declaration of competing interest

The authors declare that they have no known competing financial interests or personal relationships that could have appeared to influence the work reported in this paper.

Data availability

Data will be made available on request.

Acknowledgements

The authors acknowledge support from 1) the European Union Horizon 2020 program (project HERMES, nr. 952184), 2) the Ministry of Education, Youth and Sports of the Czech Republic for supporting CEMNAT (LM2023037) and CzechNanoLab (LM2023051) infrastructures for providing ALD, SEM, EDX, XPS, TEM and XRD accesses, 3) Czech Science Foundation (project 23-08019X, EXPRO).

Appendix A. Supplementary data

Supplementary data to this article can be found online at https://doi.org/10.1016/j.cej.2024.148959.

References

[1] N.A. Kelly, Hydrogen production by water electrolysis, Woodhead Publishing Limited (2014), https://doi.org/10.1533/9780857097736.2.159.
[2] V.R. Stamenkovic, D. Strmcnik, P.P. Lopes, N.M. Markovic, Energy and fuels from electrochemical interfaces, Nat. Mater. 16 (1) (2016) 57–69, https://doi.org/10.1038/nmat4738.
[3] J. Durst, A. Siebel, C. Simon, F. Hasché, J. Herranz, H.A. Gasteiger, New insights into the electrochemical hydrogen oxidation and evolution reaction mechanism, Energy Environ. Sci. 7 (7) (2014) 2255–2260, https://doi.org/10.1039/c4ee00440j.
[4] J. Zheng, W. Sheng, Z. Zhuang, B. Xu, Y. Yan, Universal dependence of hydrogen oxidation and evolution reaction activity of platinum-group metals on PH and hydrogen binding energy, Sci. Adv. 2 (3) (2016) 1–9, https://doi.org/10.1126/sciadv.1501602.
[5] V.S. Bagotzky, N.V. Osetrova, Investigation of hydrogen ionization on platinum with the help of micro-electrodes, J. Electroanal. Chem. 43 (2) (1973) 233–249, https://doi.org/10.1016/S0022-0728(73)80494-2.
[6] S.K. Park, D.Y. Chung, D. Ko, Y.E. Sung, Y. Piao, Three-dimensional carbon foam/N-doped graphene@MoS2 hybrid nanostructures as effective electrocatalysts for the hydrogen evolution reaction, J. Mater. Chem. A 4 (33) (2016) 12720–12725, https://doi.org/10.1039/c6ta03458f.
[7] H. Jin, S. Sultan, M. Ha, J.N. Tiwari, M.G. Kim, K.S. Kim, Simple and scalable mechanochemical synthesis of noble metal catalysts with single atoms toward highly efficient hydrogen evolution, Adv. Funct. Mater. 30 (25) (2020) 2–7, https://doi.org/10.1002/adfm.202000531.
[8] W. Sheng, H.A. Gasteiger, Y. Shao-Horn, Hydrogen oxidation and evolution reaction kinetics on platinum: acid vs alkaline electrolytes, J. Electrochem. Soc. 157 (11) (2010) B1529, https://doi.org/10.1149/1.3483106.
[9] J.N. Tiwari, N.K. Dang, S. Sultan, P. Thangavel, H.Y. Jeong, K.S. Kim, Multi-heteroatom-doped carbon from waste-yeast biomass for sustained water splitting, Nat. Sustain. 3 (7) (2020) 556–563, https://doi.org/10.1038/s41893-020-0509-6.
[10] M. Duan, T. Shu, J. Li, D. Zhang, L.Y. Gan, K.X. Yao, Q. Yuan, Boosting alkaline hydrogen evolution performance by constructing ultrasmall Ru clusters/Na+, K+-decorated porous carbon composites, Nano Res. 16 (7) (2023) 8836–8844, https://doi.org/10.1007/s12274-023-5558-5.
[11] B.S. Kalanoor, H. Seo, S.S. Kalanur, Recent developments in photoelectrochemical water-splitting using WO 3 /BiVO 4 heterojunction photoanode: a review, Mater. Sci. Energy Technol. 1 (1) (2018) 49–62, https://doi.org/10.1016/j.mset.2018.03.004.
[12] S.M. Thalluri, J. Rodriguez-Pereira, R. Zazpe, B. Bawab, E. Kolíbalová, L. Jelinek, J. M. Macak, Enhanced C-O functionality on carbon papers ensures lowering nucleation delay of ALD for Ru towards unprecedented alkaline HER activity, Small 19 (32) (2023) 1–8, https://doi.org/10.1002/smll.202300974.
[13] N.K. Dang, M. Umer, P. Thangavel, S. Sultan, J.N. Tiwari, J.H. Lee, M.G. Kim, K. S. Kim, Surface Enrichment of iridium on IrCo alloys for boosting hydrogen production, J. Mater. Chem. A 9 (31) (2021) 16898–16905, https://doi.org/10.1039/d1ta02597j.
[14] S. Sultan, M.H. Diorizky, M. Ha, J.N. Tiwari, H. Choi, N.K. Dang, P. Thangavel, J. H. Lee, H.Y. Jeong, H.S. Shin, Y. Kwon, K.S. Kim, Modulation of Cu and Rh single-atoms and nanoparticles for high-performance hydrogen evolution activity in acidic media, J. Mater. Chem. A 9 (16) (2021) 10326–10334, https://doi.org/10.1039/d1ta01067k.
[15] N. Mahmood, Y. Yao, J.W. Zhang, L. Pan, X. Zhang, J.J. Zou, Electrocatalysts for hydrogen evolution in alkaline electrolytes: mechanisms, challenges, and prospective solutions, Adv. Sci. 5 (2) (2018), https://doi.org/10.1002/advs.201700464.
[16] E. Zoulias, E. Varkaraki, N. Lymberopoulos, C.N. Christodoulou, G.N. Karagiorgis, A review on water electrolysis, Tcjst 4 (2) (2004) 41–71.
[17] R.Q. Yao, Y.T. Zhou, H. Shi, Q.H. Zhang, L. Gu, Z. Wen, X.Y. Lang, Q. Jiang, Nanoporous palladium-silver surface alloys as efficient and PH-universal catalysts for the hydrogen evolution reaction, ACS Energy Lett. 4 (6) (2019) 1379–1386, https://doi.org/10.1021/acsenergylett.9b00845.
[18] J. Ge, P. Wei, G. Wu, Y. Liu, T. Yuan, Z. Li, Y. Qu, Y. Wu, H. Li, Z. Zhuang, X. Hong, Y. Li, Ultrathin palladium nanomesh for electrocatalysis, Angew. Chemie - Int. Ed. 57 (13) (2018) 3435–3438, https://doi.org/10.1002/anie.201800552.
[19] F.H.B. Lima, J. Zhang, M.H. Shao, K. Sasaki, M.B. Vukmirovic, E.A. Ticianelli, R. R. Adzic, Catalytic activity - d-band center correlation for the O2 reduction reaction on platinum in alkaline solutions, J. Phys. Chem. C 111 (1) (2007) 404–410, https://doi.org/10.1021/jp065181r.
[20] C. Zhang, Z. Zhou, X. Wang, J. Liu, J. Sun, L. Wang, et al., Synergy between Palladium Single Atoms and Small Nanoparticles Co-Anchored on Carbon Atom Self-Doped Graphitic Carbon Nitride Boosting Photocatalytic H2 Generation.
[21] Y. Lu, J. Wang, Y. Peng, A. Fisher, X. Wang, Highly efficient and durable Pd Hydride nanocubes embedded in 2D amorphous NiB nanosheets for oxygen reduction reaction, Adv. Energy Mater. 7 (21) (2017) 1–7, https://doi.org/10.1002/aenm.201700919.
[22] H. Lv, X. Chen, D. Xu, Y. Hu, H. Zheng, S.L. Suib, B. Liu, Ultrathin PdPt bimetallic nanowires with enhanced electrocatalytic performance for hydrogen evolution reaction, Appl. Catal. B Environ. 238 (2018) 525–532, https://doi.org/10.1016/j.apcatb.2018.07.060.
[23] S. Liu, X. Mu, H. Duan, C. Chen, H. Zhang, Pd nanoparticle assemblies as efficient catalysts for the hydrogen evolution and oxygen reduction reactions, Eur. J. Inorg. Chem. 2017 (3) (2017) 535–539, https://doi.org/10.1002/ejic.201601277.
[24] Y. Jia, T.H. Huang, S. Lin, L. Guo, Y.M. Yu, J.H. Wang, K.W. Wang, S. Dai, Stable Pd-Cu hydride catalyst for efficient hydrogen evolution, Nano Lett. 22 (3) (2022) 1391–1397, https://doi.org/10.1021/acs.nanolett.1c04840.
[25] J. Zheng, S. Zhou, S. Gu, B. Xu, Y. Yan, Size-dependent hydrogen oxidation and evolution activities on supported palladium nanoparticles in acid and base, J. Electrochem. Soc. 163 (6) (2016) F499–F506, https://doi.org/10.1149/2.0661606jes.
[26] K. Gu, F. Wei, Y. Cai, S. Lin, H. Guo, Dynamics of initial hydrogen spillover from a single atom platinum active site to the Cu(111) host surface: the impact of

substrate electron-hole pairs, J. Phys. Chem. Lett. 12 (34) (2021) 8423–8429, https://doi.org/10.1021/acs.jpclett.1c02019.
[27] H. Shen, H. Li, Z. Yang, C. Li, Magic of hydrogen spillover: understanding and application, Green Energy Environ. 7 (6) (2022) 1161–1198, https://doi.org/10.1016/j.gee.2022.01.013.
[28] U. Petek, F. Ruiz-Zepeda, M. Bele, M. Gaberšček, Nanoparticles and single atoms in commercial carbon-supported platinum-group metal catalysts, Catalysts 9 (2) (2019), https://doi.org/10.3390/catal9020134.
[29] W. Xu, M. Cao, J. Luo, H. Mao, H. Gu, Z. Sun, Q. Liu, S. Zhang, Research progress on single atom and particle synergistic catalysts for electrocatalytic reactions, Mater. Chem. Front. 7 (10) (2023) 1992–2013, https://doi.org/10.1039/d2qm01352e.
[30] C.B. Thompson, Y. Lu, A.M. Karim, Kinetic synergy between supported Ir single atoms and nanoparticles during CO oxidation light-off, Ind. Eng. Chem. Res. 60 (44) (2021) 15960–15971, https://doi.org/10.1021/acs.iecr.1c02806.
[31] W. Zhou, J. Jia, J. Lu, L. Yang, D. Hou, G. Li, S. Chen, Recent developments of carbon-based electrocatalysts for hydrogen evolution reaction, Nano Energy 28 (2016) 29–43, https://doi.org/10.1016/j.nanoen.2016.08.027.
[32] L. Zhang, J. Xiao, H. Wang, M. Shao, Carbon-based electrocatalysts for hydrogen and oxygen evolution reactions, ACS Catal. 7 (11) (2017) 7855–7865, https://doi.org/10.1021/acscatal.7b02718.
[33] I. Dumitrescu, P.R. Unwin, J.V. MacPherson, Electrochemistry at carbon nanotubes: perspective and issues, Chem. Commun. 7345 (45) (2009) 6886–6901, https://doi.org/10.1039/b909734a.
[34] J.P. Chen, S. Wu, Acid/base-treated activated carbons: characterization of functional groups and metal adsorptive properties, Langmuir 20 (6) (2004) 2233–2242, https://doi.org/10.1021/la0348463.
[35] Y.J. Kang, H.K. Jo, M.H. Jang, G.J. Han, S.J. Yoon, K. Oh, J.I. Park, Acid Treatment Enhances Performance of Beads Activated Carbon for Formaldehyde Removal 33 (2023) 397–408.
[36] J.J. Senkevich, F. Tang, D. Rogers, J.T. Drotar, C. Jezewski, W.A. Lanford, G. C. Wang, T.M. Lu, Substrate-independent palladium atomic layer deposition, Chem. Vap. Depos. (2003) 258–264, https://doi.org/10.1002/cvde.200306246.
[37] G. Zhang, S. Sun, D. Yang, J.P. Dodelet, E. Sacher, The surface analytical characterization of carbon fibers functionalized by H2SO4/HNO3 Treatment, carbon NY. 46 (2) (2008) 196–205, https://doi.org/10.1016/j.carbon.2007.11.002.
[38] J.Y. Feng, R.K. Ramachandran, E. Solano, M.M. Minjauw, M. Van Daele, A. Vantomme, D. Hermida-Merino, A. Coati, H. Poelman, C. Detavernier, J. Dendooven, Tuning Size and coverage of Pd nanoparticles using atomic layer deposition, Appl. Surf. Sci. 2021 (August 2020) 539, https://doi.org/10.1016/j.apsusc.2020.148238.
[39] J.W. Elam, A. Zinovev, C.Y. Han, H.H. Wang, U. Welp, J.N. Hryn, M.J. Pellin, Atomic layer deposition of palladium films on Al2O3 surfaces, Thin Solid Films 515 (4) (2006) 1664–1673, https://doi.org/10.1016/j.tsf.2006.05.049.
[40] J.L. Figueiredo, M.F.R. Pereira, M.M.A. Freitas, J.J.M. Órfão, Characterization of active sites on carbon catalysts, Ind. Eng. Chem. Res. 46 (12) (2007) 4110–4115, https://doi.org/10.1021/ie061071v.
[41] D.N. Goldstein, S.M. George, Surface poisoning in the nucleation and growth of palladium atomic layer deposition with Pd(Hfac)2 and formalin, Thin Solid Films 519 (16) (2011) 5339–5347, https://doi.org/10.1016/j.tsf.2011.02.037.
[42] N. Cheng, S. Stambula, D. Wang, M.N. Banis, J. Liu, A. Riese, B. Xiao, R. Li, T. K. Sham, L.M. Liu, G.A. Botton, X. Sun, Platinum single-atom and cluster catalysis of the hydrogen evolution reaction, Nat. Commun. 7 (1) (2016) 13638, https://doi.org/10.1038/ncomms13638.
[43] M.T.X. Nguyen, M.K. Nguyen, P.T.T. Pham, H.K.P. Huynh, H.H. Pham, C.C. Vo, S. T. Nguyen, High-performance Pd-coated Ni nanowire electrocatalysts for alkaline direct ethanol fuel cells, J. Electroanal. Chem. 888 (March) (2021) 115180, https://doi.org/10.1016/j.jelechem.2021.115180.
[44] M. Brun, A. Berthet, J.C. Bertolini, XPS, AES and auger parameter of Pd and PdO, J. Electron Spectros. Relat. Phenomena 104 (1–3) (1999) 55–60, https://doi.org/10.1016/s0368-2048(98)00312-0.
[45] H. Yan, H. Cheng, H. Yi, Y. Lin, T. Yao, C. Wang, J. Li, S. Wei, J. Lu, Single-atom Pd 1 /graphene catalyst achieved by atomic layer deposition: remarkable performance in selective hydrogenation of 1,3-butadiene, J. Am. Chem. Soc. 137 (33) (2015) 10484–10487, https://doi.org/10.1021/jacs.5b06485.
[46] G. Cha, I. Hwang, S. Hejazi, A.S. Dobrota, I.A. Pašti, B. Osuagwu, H. Kim, J. Will, T. Yokosawa, Z. Badura, Š. Kment, S. Mohajernia, A. Mazare, N.V. Skorodumova, E. Spiecker, P. Schmuki, As a single atom Pd outperforms Pt as the most active co-catalyst for photocatalytic H2, Evolution 24 (8) (iScience 2021,), https://doi.org/10.1016/j.isci.2021.102938.
[47] D. Bhalothia, T.H. Huang, P.H. Chou, K.W. Wang, T.Y. Chen, Promoting formic acid oxidation performance of Pd nanoparticlesviapt and Ru atom mediated surface engineering, RSC Adv. 10 (29) (2020) 17302–17310, https://doi.org/10.1039/d0ra01303j.
[48] R. Westerström, C.J. Weststrate, J. Gustafson, A. Mikkelsen, J. Schnadt, J. N. Andersen, E. Lundgren, N. Seriani, F. Mittendorfer, G. Kresse, A. Stierle, Lack of surface oxide layers and facile bulk oxide formation on Pd(110), Phys. Rev. B - Condens. Matter Mater. Phys. 80 (12) (2009) 1–11, https://doi.org/10.1103/PhysRevB.80.125431.
[49] R. Westerström, M.E. Messing, S. Blomberg, A. Hellman, H. Grönbeck, J. Gustafson, N.M. Martin, O. Balmes, R. Van Rijn, J.N. Andersen, K. Deppert, H. Bluhm, Z. Liu, M.E. Grass, M. Hävecker, E. Lundgren, Oxidation and reduction of Pd(100) and aerosol-deposited Pd nanoparticles, Phys. Rev. B - Condens. Matter Mater. Phys. 83 (11) (2011) 1–10, https://doi.org/10.1103/PhysRevB.83.115440.
[50] X. Cheng, Z. Wang, Y. Mao, P. Hu, Evidence of the O-Pd-O and Pd-O4 structure units as oxide seeds and their origin on Pd(211): revealing the mechanism of surface oxide formation, Phys. Chem. Chem. Phys. 21 (12) (2019) 6499–6505, https://doi.org/10.1039/c8cp06224b.
[51] S. Yu, X. Cheng, Y. Wang, B. Xiao, Y. Xing, J. Ren, Y. Lu, H. Li, C. Zhuang, G. Chen, High activity and selectivity of single palladium atom for oxygen hydrogenation to H2O2, Nat. Commun. 13 (1) (2022) 1–9, https://doi.org/10.1038/s41467-022-32450-6.
[52] X. Zhao, X. Li, D. Xiao, M. Gong, L. An, P. Gao, J. Yang, D. Wang, Isolated Pd atom anchoring endows cobalt diselenides with regulated water-reduction kinetics for alkaline hydrogen evolution, Appl. Catal. B Environ. 295 (2021) 120280, https://doi.org/10.1016/j.apcatb.2021.120280.
[53] T. Jiang, L. Yu, Z. Zhao, W. Wu, Z. Wang, N. Cheng, Regulating the intermediate affinity on Pd nanoparticles through the control of inserted-B atoms for alkaline hydrogen evolution, Chem. Eng. J. 433 (P2) (2022) 133525, https://doi.org/10.1016/j.cej.2021.133525.
[54] R. Tan, D. Wu, S. Xu, Y. Zhu, D. Xiong, L. Wang, P. Yang, P.K. Chu, Electrocatalytic hydrogen evolution of palladium nanoparticles electrodeposited on nanographene coated macroporous electrically conductive network, Int. J. Hydrogen Energy 43 (4) (2018) 2171–2183, https://doi.org/10.1016/j.ijhydene.2017.12.064.
[55] G. Valenti, A. Boni, M. Melchionna, M. Cargnello, L. Nasi, G. Bertoni, R.J. Gorte, M. Marcaccio, S. Rapino, M. Bonchio, P. Fornasiero, M. Prato, F. Paolucci, Co-axial heterostructures integrating palladium/titanium dioxide with carbon nanotubes for efficient electrocatalytic hydrogen evolution, Nat. Commun. 7 (2016) 1–8, https://doi.org/10.1038/ncomms13549.
[56] T. Shinagawa, A.T. Garcia-Esparza, K. Takanabe, Insight on tafel slopes from a microkinetic analysis of aqueous electrocatalysis for energy conversion, Sci. Rep. 5 (May) (2015) 1–21, https://doi.org/10.1038/srep13801.
[57] P. Liu, Z. Huang, X. Gao, X. Hong, J. Zhu, G. Wang, Y. Wu, J. Zeng, X. Zheng, Synergy between palladium single atoms and nanoparticles via hydrogen spillover for enhancing CO2 photoreduction to CH4, Adv. Mater. 34 (16) (2022) 1–11, https://doi.org/10.1002/adma.202200057.
[58] J. Li, J. Hu, M. Zhang, W. Gou, S. Zhang, Z. Chen, Y. Qu, Y. Ma, A Fundamental viewpoint on the hydrogen spillover phenomenon of electrocatalytic hydrogen evolution, Nat. Commun. 12 (1) (2021) 1–12, https://doi.org/10.1038/s41467-021-23750-4.
[59] C. Wei, R.R. Rao, J. Peng, B. Huang, I.E.L. Stephens, M. Risch, Z.J. Xu, Y. Shao-Horn, Recommended practices and benchmark activity for hydrogen and oxygen electrocatalysis in water splitting and fuel cells, Adv. Mater. 31 (31) (2019) 1–24, https://doi.org/10.1002/adma.201806296.
[60] L.L. Fang, Q. Tao, M.F. Li, L.W. Liao, D. Chen, Y.X. Chen, Determination of the real surface area of palladium electrode, Chinese J. Chem. Phys. 23 (5) (2010) 543–548, https://doi.org/10.1088/1674-0068/23/05/543-548.
[61] L. Yang, Y. Tang, S. Luo, C. Liu, H. Song, D. Yan, Palladium nanoparticles supported on vertically oriented reduced graphene oxide for methanol electro-oxidation, ChemSusChem 7 (10) (2014) 2907–2913, https://doi.org/10.1002/cssc.201402352.
[62] J. Shu, R. Li, Z. Lian, W. Zhang, R. Jin, H. Yang, S. Li, In-situ oxidation of palladium-iridium nanoalloy anchored on nitrogen-doped graphene as an efficient catalyst for methanol electrooxidation, J. Colloid Interface Sci. 605 (2022) 44–53, https://doi.org/10.1016/j.jcis.2021.07.056.
[63] K. Naga Mahesh, R. Balaji, K.S. Dhathathreyan, Palladium nanoparticles as hydrogen evolution reaction (HER) electrocatalyst in electrochemical methanol reformer, Int. J. Hydrogen Energy 41 (1) (2016) 46–51, https://doi.org/10.1016/j.ijhydene.2015.09.110.
[64] D. Voiry, M. Chhowalla, Y. Gogotsi, N.A. Kotov, Y. Li, R.M. Penner, R.E. Schaak, P. S. Weiss, Best practices for reporting electrocatalytic performance of nanomaterials, ACS Nano 12 (10) (2018) 9635–9638, https://doi.org/10.1021/acsnano.8b07700.
[65] C. Costentin, G. Passard, J.M. Savéant, Benchmarking of homogeneous electrocatalysts: overpotential, turnover frequency, limiting turnover number, J. Am. Chem. Soc. 137 (16) (2015) 5461–5467, https://doi.org/10.1021/jacs.5b00914.
[66] M. Batool, A. Hameed, M.A. Nadeem, Recent developments on iron and nickel-based transition metal nitrides for overall water splitting: a critical review, Coord. Chem. Rev. 480 (2023) 215029, https://doi.org/10.1016/j.ccr.2023.215029.